Effects of air chemistry and stiffened EOS of air in numerical simulations of bubble collapse in water

J. Zhang,[1,*] T. L. Jackson,[2,†] and A. M. D. Jost[1,‡]

[1]*Department of Mechanical and Aerospace Engineering, F. W. Olin Engineering, 251, 150 West University Blvd., Florida Institute of Technology, Melbourne, Florida 32901, USA*

[2]*Department of Mechanical and Aerospace Engineering, Particle Science and Technology, Building 0746 Room 205B, 1180 Center Drive, University of Florida, Gainesville, Florida 32611, USA*

(Received 6 January 2017; published 25 May 2017)

In this paper we study the effects of a stiffened gas equation of state for air at high pressure and air chemistry with dissociation in numerical simulations of bubble collapse in water. Two types of bubble collapse are studied, with one corresponding to spherically symmetric collapse simulating single-bubble sonoluminescence (SBSL), and the other a GPa-shock-induced axisymmetric bubble collapse. The numerical method is a finite-volume based solver with diffuse material interface model. Verification and validation of the solver are demonstrated by comparing to analytical solutions and experimental observations. We find that for sonoluminescence, air chemistry and equation of state for air at high pressures can have significant effects on the peak temperature and pressure attained during the evolution, and that the peak temperature is on the order of 1 eV, which is close to that observed in experiments. For shock-induced bubble collapse, the pressure inside the bubble will not be as high as that in sonoluminescence due to the absence of spherical symmetry. However, the air chemistry still has a significant effect on the temperature of the bubble. We also examine the effect of multiple bubble interaction in shock-induced bubble collapse and find several mechanisms that can significantly increase the pressure in the water. These mechanisms include frontal-distal-side-collision, shock focusing, upstream-traveling shocks, and compression of the water near the centerline by the vortex generated by bubble collapse. These have important implications for cavitation erosion.

DOI: 10.1103/PhysRevFluids.2.053603

I. INTRODUCTION

Sonoluminescence and cavitation erosion are two closely related phenomena that were discovered about the same time nearly 100 years ago. The study of cavitation erosion started with the finding of severe destructive effects on the propellers of the great ocean liners *Lusitania and Mauretania*, reported first by Silberrad [1] in 1912, while sonoluminescence was first discovered in 1933 by Marinesco and Trillat [2], who noted that photographic plates immersed in water fogged when irradiated by ultrasound. The next year Frenzel and Schultes [3] directly observed sonoluminescence in water. The highly unwanted destructive effect in cavitation erosion appears wherever high-pressure gradients or large flow rates lead to the generation of bubbles in the vicinity of a solid boundary. It not only causes damage to propellers but limits the efficiency of hydraulic machinery like turbines or pumps. On the other hand, the ability to create and trap a single bubble sonoluminescence in a laboratory setting by Gaittan [4] caused a renaissance in sonoluminescence [5]; interest in single-bubble and multi-bubble sonoluminescence (SBSL and MBSL, respectively) for medical, environmental, chemical, and mechanical reasons has also

*jzhang@fit.edu
†tlj@ufl.edu
‡ajost2009@my.fit.edu

increased. Sonoluminescence involves the conversion of acoustical to optical energy. Through the application of an acoustic field, a bubble can be created by the expansion wave of the sound field. The bubble will grow and contract with the cycling of the acoustic field. With acoustic fields of sufficient amplitude, the expansion and compression cycle becomes highly nonlinear. The runaway inertial collapse and compression of bubble contents lead to a flash of light that lasts tens of picoseconds to a few nanoseconds. The conditions inside the bubble can be extreme. Temperatures inside the bubble can reach 15 000 K, and pressures can reach GPa. The two phenomena share many key similarities. Both involve highly nonlinear bubble dynamics and bubble collapse with pressures reaching as high as GPa and temperatures on the order of eV (1 eV = 11 605 K); see Refs. [6,7] and references therein. Despite the discovery of both phenomena nearly a century ago, the fundamental mechanisms that contribute to either phenomenon are not very well understood.

The emission of high-pressure pulses by a collapsing bubble, which originates from a strong compression of the bubble contents, has been well known since the famous theoretical work of Rayleigh [8] on an imploding spherical cavity. Developed by Rayleigh [8] and refined by Plesset [9], the Rayleigh-Plesset (R-P) model is one of the most predominant models used to describe sonoluminescence. Improvements to the P-R model by incorporating sound radiation, van der Waals hard core law, and retarded time has resulted in advanced models such as Gilmore and Keller-Miksis (K-M) [10]. The underlying assumptions of P-R are also presented in these more advanced models; the accuracy of the models for bubble motion away from maximum compression and collapse is better. However, the theoretical work becomes insufficient since the assumptions depart from the actual bubble conditions at times of maximum compression. One such assumption is that the density of the liquid is much larger than the gas density within the bubble, which is not true during the bubble collapse when the bubble approaches the minimum radius for a strongly driven bubble. There are abundant numerical studies that solve the P-R model with various physical and chemical processes included [11–17]. Yasui [11] and Yasui *et al.* [12] extended the P-R-based model to include vapor and air chemistry, dissolution, vaporization and condensation, etc. Schanz *et al.* studied the sonochemistry using a combination of R-P and molecular dynamics (MD). Prosperetti reviewed the fundamental physics of vapor bubbles in liquids [15].

Full hydrodynamic numerical simulations of SBSL with the compressible equations do not have the limitations of P-R model, yet the amount of these simulations is severely limited. To the best of our knowledge, Wu and Roberts [18] and Moss *et al.* [19] are among the first attempts at a full hydrodynamic simulation of SBSL. Recently, Koch *et al.* [20] modified the finite volume Navier-Stokes solver and the two-phase solver in OpenFoam to simulate the dynamics of laser-generated bubbles. On the other hand, significantly more full hydrodynamic simulations were performed for interaction of a bubble and a shockwave for the obvious reason that the complexity in these interaction defies concise analytical treatment; see Refs. [21–24] and references therein. This leaves numerical methods as the foremost means of studying shock-bubble interaction and cavitation erosion.

None of the above cited work on full hydrodynamic numerical simulations of SBSL include air chemistry explicitly in the governing equations. As a result, the simulated temperatures inside the bubble reaches as high as $\sim$100 eV in numerical simulations of SBSL. It will be shown in the current work that when air chemistry is included, the bubble temperature is reduced to be on the order of 1 eV, which is closer to that observed in sonoluminescence experiments. In addition, the pressures in sonoluminescence reach as high as GPa with the presence of an imposed shock, and the simulated density is on the order of $\sim$1000 kg/m^3. Thus, a stiffened-gas equation of state (EOS) calibrated by shock Hugoniot data of liquid air in Ref. [25] is expected to be relevant at high pressures. To our knowledge, the effect of a stiffened EOS for air at high pressures has not been explored and examined numerically before. It will be demonstrated here that with a stiffened EOS of air at high pressures, the peak pressure is reduced by an order of magnitude.

The paper is organized as follows. The governing equations and numerical method are presented in Sec. II. Verification of the numerical method is presented in Sec. III. The results are presented

in Sec. IV for sonoluminescence and shock-bubble interaction. Finally, conclusions are given in Sec. V.

II. FORMULATIONS

In the present study we ignore the effects of thermal and mass diffusion, surface tension, and radiation. Thus, the governing equations for a reactive compressible medium are given by

$$\frac{\partial \rho}{\partial t} + \nabla \cdot (\rho \boldsymbol{u}) = 0, \tag{1}$$

$$\frac{\partial (\rho \boldsymbol{u})}{\partial t} + \nabla p + \nabla \cdot (\rho \boldsymbol{u}\boldsymbol{u}) = 0, \tag{2}$$

$$\frac{\partial E}{\partial t} + \nabla \cdot [(E + p)\boldsymbol{u}] = \Sigma Q_i \Omega_i, \tag{3}$$

$$\frac{\partial (\rho Y_i)}{\partial t} + \nabla \cdot (\rho \boldsymbol{u} Y_i) = -\Omega_i, \tag{4}$$

where ρ is the density, $\boldsymbol{u}$ the velocity, p the pressure,

$$E = \rho\left(e + \tfrac{1}{2}\boldsymbol{u} \cdot \boldsymbol{u}\right), \tag{5}$$

the total energy per unit volume, Y_i the mass fraction of the ith reactant, and Q_i a heat release parameter. The chemistry model is presented in Sec. II C. The system is closed by adding an appropriate EOS,

$$p = p(\rho, e). \tag{6}$$

The EOS can be an ideal gas EOS, a stiffened EOS, or a Mie-Gruneisen EOS. In this work the EOS for water is a stiffened EOS, and that for air is ideal when the local pressure is below 1 GPa but stiffened when the local pressure is above 1 GPa.

The Euler equations (1)–(4) are solved in conservative form using the common reconstruct-and-evolve strategy within a finite-volume framework. In addition, a Total Variation Diminishing (TVD) reconstruction with the Minmod limiter [26] is employed. The Harten-Lax–van Leer–with-Contact (HLLC) approximate Riemann solver [27] is chosen for its good resolution of shocks and its positivity of density and internal energy. Time integration is performed using a strong-stability-preserving third-order Runge-Kutta method [28]. See Shukla *et al.* [29] for more details.

A. Diffuse interface model

The particular problems we are addressing can have detonations, shock waves, and material interfaces, and therefore an appropriate numerical method must be capable of handling all of them. A numerical method was recently developed by Shukla *et al.* for handling such problems [29], albeit in the absence of chemistry. Extension to reactive flow was done in Ref. [30].

A key ingredient in multimaterial modeling in Ref. [29] is the use of a material marker ϕ, advected according to

$$\frac{\partial \phi_k}{\partial t} + \mathbf{u} \cdot \nabla \phi_k = 0. \tag{7}$$

Here ϕ_k is the volume fraction of material k, such that $\sum \phi_k = 1$. In the physical system ϕ_k jumps from 0 to 1 across a material interface, but in the numerical scheme it changes smoothly over a small number of mesh points, a set S. Over a time step Δt, ϕ_k is advanced using Eq. (7). Upwind fluxes for the advection equation for the interface function ϕ_k are calculated as a part of the two-fluid Riemann problem using the contact velocity from the HLLC solver.

TABLE I. Parameters of the stiffened-gas EOS.

Parameter	Water	Air ($p_{\max} \leqslant 1$ GPa)	Air ($p_{\max} > 1$ GPa)
ρ_0 (kg/m^3)	1000	1	1000
γ	4.4	1.4	2.6
P^∞ (atm)	6000	0	1.07×10^4

Over a time step Δt, ϕ is advected using (7), but before moving to the next time step a correction is calculated on $\mathcal{S}$ by means of the equation

$$\frac{\partial \phi}{\partial \hat{\tau}} = \hat{n} \cdot \nabla[\epsilon_h |\nabla \phi| - \phi(1-\phi)], \tag{8}$$

where $\epsilon_h = 0.5h$ with h being the grid resolution, $\hat{\tau}$ is a pseudotime, and $\hat{n}$ is the interface normal. This equation is integrated to steady state in $\hat{\tau}$. The nonlinear term leads to convective steepening of the interface region, whereas the diffusion term smears it out; these effects balance, as in Burger's equation.

The density ρ is treated in a similar fashion using

$$\frac{\partial \rho}{\partial \hat{\tau}} = H(\phi)\hat{n} \cdot [\nabla(\epsilon_h \hat{n} \cdot \nabla \rho) - (1-2\phi)\nabla \rho], \tag{9}$$

where

$$H(\phi) = \tanh\left\{\left[\frac{\phi(1-\phi)}{10^{-2}}\right]^2\right\}. \tag{10}$$

The Heaviside function $H(\phi)$ ensures that the density correction step is limited to the interface region. This scheme was fully demonstrated in Ref. [29] and for reacting flows in Ref. [30]; see also Refs. [31–33].

B. Equation of state

A stiffened-gas EOS is used for closure and is given by

$$\rho_k e_k = \Gamma_k p_k + \Pi_k, \tag{11}$$

with

$$\Pi_k = \frac{\gamma_k p_k^\infty}{\gamma_k - 1}, \quad \Gamma_k = \frac{1}{\gamma_k - 1}. \tag{12}$$

Here γ is a parameter and p^∞ is a constant. Both can be calibrated for a certain material. Note that in the limit $p^\infty \to 0$ the stiffened EOS reduces to the ideal EOS and γ becomes the ratio of specific heats.

With the volume fraction ϕ known, the EOS parameters of the mixture can then be obtained. The isobaric closure of Allaire *et al.* [34] was chosen in Ref. [29] for stiffened EOS parameters. This leads to the following mixture rules for a two-material smeared interface:

$$\Gamma = \phi\Gamma_1 + (1-\phi)\Gamma_2,$$
$$\Pi = \phi\Pi_1 + (1-\phi)\Pi_2.$$

Extension to multimaterials is straightforward.

The EOS parameters for the materials in the current work are listed in Table I. Note that we assume in this work that the EOS for the air inside the bubble at pressures on the order of GPa and

TABLE II. Kinetic parameters of O_2 and N_2 dissociation; see Ref. [35], and see Ref. [36] for values of Q.

	O_2	N_2
$\mathcal{M}$ (g/mol)	32	28
C_f ($\frac{\text{cm}^3\,\text{K}^{-\eta_f}}{\text{mol s}}$)	3.24×10^{19}	4.7×10^{17}
η_f	-1	-0.5
K_f (cal/mol)	119 000	226 000
$\mathcal{R}$ (cal/mol K)	1.986	1.986
Q (MJ/kg)	-15.56	-33.79

larger is stiffened. The calibration of the parameters is based on shock Hugoniot data of liquid N_2 in Ref. [25]. The use of shock data seems plausible in the current problem in which shocks with pressures on the order of GPa are present.

C. Air chemistry

The model of air chemistry at high temperature is based on Ref. [35]. In the current work, only dissociation of N_2 and O_2 are modeled since they are the most significant for the present discussion. For dissociation of O_2, we have

$$O_2 + M \xrightarrow{k_f} 2O + M, \tag{13}$$

with reaction rate

$$\frac{d[O]}{dt} = 2k_f[O_2][M] \tag{14}$$

or

$$\frac{d[O_2]}{dt} = -k_f[O_2][M]. \tag{15}$$

In this work, the collision partner M is chosen to be O_2, and the reaction rate is then written in terms of mass fraction of O_2, Y_{O_2}, as

$$\frac{d(\rho Y_{O_2}/\mathcal{M}_{O_2})}{dt} = -k_f(\rho Y_{O_2}/\mathcal{M}_{O_2})^2, \tag{16}$$

where

$$k_f = C_f T^{\eta_f} e^{-K_f/\mathcal{R}T}, \tag{17}$$

with parameters listed in Table II. Thus, the source term for O_2 in Eq. (4) is given by

$$\Omega = k_f(\rho Y_{O_2})^2/\mathcal{M}_{O_2}. \tag{18}$$

For dissociation of N_2, the model is exactly the same as that for O_2 but with the collision partner M chosen to be N_2. Thus,

$$\frac{d(\rho Y_{N_2}/\mathcal{M}_{N_2})}{dt} = -k_f(\rho Y_{N_2}/\mathcal{M}_{N_2})^2, \tag{19}$$

$$k_f = C_f T^{\eta_f} e^{-K_f/\mathcal{R}T}, \quad \Omega = k_f(\rho Y_{N_2})^2/\mathcal{M}_{N_2}. \tag{20}$$

The parameters are also listed in Table II.

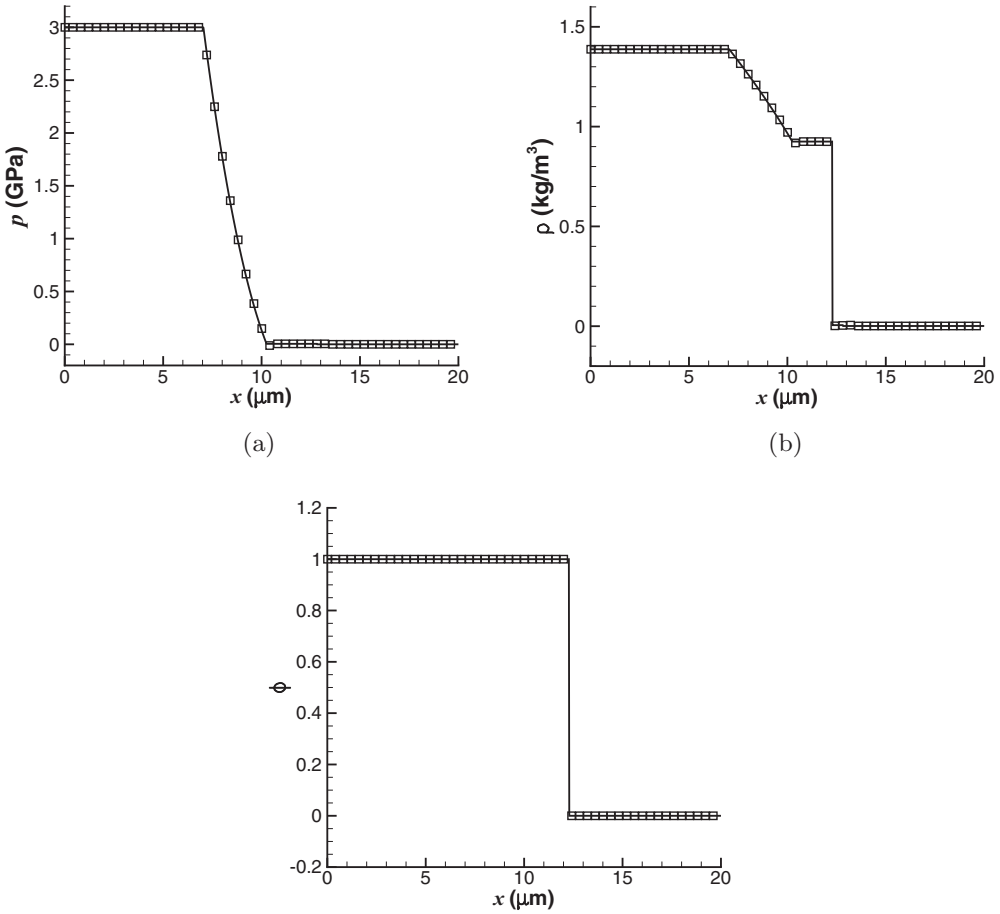

FIG. 1. Plot of (a) pressure, (b) density, and (c) volume fraction ϕ as a function of x for exact (solid) and numerical (symbol) solution of shock water-air interface interaction in 1D planar geometry at $t = 0.0012$ μs and $p_s = 3$ GPa in water. The number of grid points is 1000.

III. VERIFICATION

To verify the shock-material-interface capabilities of the code, we first consider a strong planar shock incident on a material interface of water and air. Figure 1 plots the comparison of the exact solution with the numerical solution for a shock pressure of $p_s = 3$ GPa in water. At time $t = 0$, the water-air interface is located at $x = 10$ μm, with the material being water to the left and air to the right, while the shock is also at $x = 10$ μm and subsequently will travel to the right. The initial conditions are given by

$$(\rho, u, p) = \begin{cases} (1388\ (\mathrm{kg/m^3}), 915\ (\mathrm{m/s}), 3\ (\mathrm{GPa})), & \text{for} \quad 0 \leqslant x \leqslant 10\ (\mu\mathrm{m}), \\ (1\ (\mathrm{kg/m^3}), 0\ (\mathrm{m/s}), 10^5\ (\mathrm{Pa})), & \text{for} \quad 10 < x \leqslant 20\ (\mu\mathrm{m}). \end{cases} \tag{21}$$

The exact solution is given by a Mach 6.27 (wave speed of 2346 m/s) shock wave moving to the right, a contact with density jump of 925:5.32 at 1905 m/s also moving to the right, and a left-moving expansion wave with a head speed of -2463 m/s and a tail speed of 209.5 m/s. The difference between the exact and the numerical solution is less than 1%.

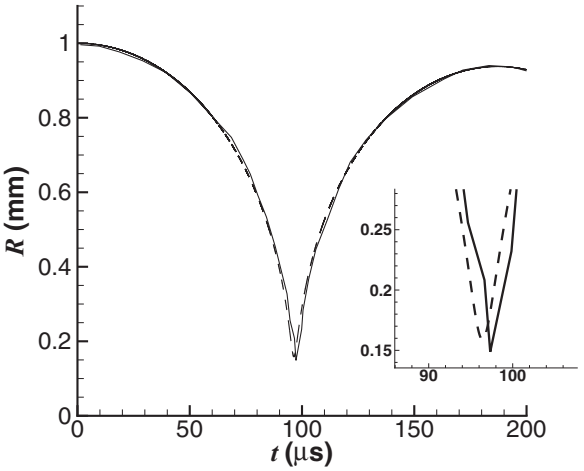

FIG. 2. Plot of bubble radius R as a function of time with an inset showing the evolution near the collapse. Here, the curves correspond to the semianalytical solution of Ref. [37] (solid) and to the current simulation (dashed). The number of grid points is 16 000.

The second verification problem is the single bubble collapse test problem considered in Ref. [31]. In this problem, the collapse of a spherical air bubble in water under an initial pressure ratio $p_\infty/p_0 = 25$, with p_∞ of 10^5 Pa and the bubble at its maximum radius $R_0 = 1$ mm at $t = 0$, is considered. The initial conditions are given by

$$\rho = \rho_1\phi + \rho_2(1-\phi), \quad u = 0, \tag{22}$$

$$p = \begin{cases} p_0, & \text{for } 0 \leqslant r \leqslant R_0, \\ p(r) = p_\infty + \frac{R_0}{r}(p_0 - p_\infty), & \text{otherwise}, \end{cases} \tag{23}$$

$$\phi = \frac{1}{2}\left[1 + \tanh\left(\frac{r - R_0}{2\epsilon_h}\right)\right], \tag{24}$$

where ϕ is the water volume fraction. Here r is the radial coordinate in spherical coordinates. The stiffened-gas EOS parameters are listed in Table I, except that the initial density ρ_0 for air in this case is set to 0.19 (kg/m^3). A domain of [0:200] mm with 16 000 grid points is used in the current simulation. The CFL number is 0.5. The solution is compared to that by [37] in Fig. 2. Excellent agreement is obtained.

IV. RESULTS

In this section we present results for two bubble collapse problems in water, namely, sonoluminescence and shock-bubble collapse.

A. Sonoluminescence

Bubble collapse in spherical symmetry corresponding to an initial bubble radius of $R_0 = 30\ \mu$m in water is simulated. The initial conditions are chosen to be representative of those for Step 2 in Ref. [19] and are given by

$$\rho = \rho_1\phi + \rho_2(1-\phi), \tag{25}$$

$$p = 10^5 \text{ (Pa)}, \tag{26}$$

$$v_r = \begin{cases} 0, & \text{for } r_0 \leqslant r \leqslant R_0, \\ -100\ (\text{m/s}), & \text{otherwise}, \end{cases} \tag{27}$$

$$\phi = \frac{1}{2}\left[1 + \tanh\left(\frac{r - R_0}{2\epsilon_h}\right)\right], \tag{28}$$

where ϕ is the water volume fraction. Here r is the radial coordinate in spherical coordinates. Note that the inner boundary of the domain is set to $r_0 = 0.05$ μm to remove the singularity at $r = 0$; our solutions are insensitive to this choice provided it is sufficiently small (results not shown). The initial mass fraction of O_2 and N_2 in the bubble are 0.233 and 0.767, respectively. The stiffened-gas EOS parameters are listed in Table I.

The computational domain is taken to be [0.05:240] μm in the radial direction. Symmetry boundary conditions and zero-gradient boundary conditions are used at the inner and outer boundaries, respectively. We note that simulations with a larger domain size was also performed, and the results found to be insensitive to it. The CFL number is 0.5.

We first perform a grid resolution study. Figure 3 plots the evolutions of radius, maximum temperature, and maximum pressure for different grid resolutions. It is seen that the solutions converge as Δr becomes smaller. To better see the evolution of bubble collapse, we show in Figure 4 plots of temperature, pressure, and mass fraction of O_2 at various times and for the grid resolution of $\Delta r = 7.5$ nm. By comparing Figs. 3 and 4, it can be seen that the first peaks in temperature and pressure correspond to the moment when the shock reaches the inner boundary of the bubble; see panel (b) of Fig. 4. The second peak corresponds to the moment of rebounding; see panel (d) of Fig. 4.

We next examine the combined effects of the EOS and air chemistry at high pressures inside the bubble. Two cases are simulated. Case A includes both stiffened gas EOS at high pressure and air chemistry, whereas case B does not. Figure 5 plots the bubble radius, maximum temperature, and maximum pressure as a function of time and for both cases A and B. It can be seen from the figure that air chemistry and the EOS at high pressure has a significant effect on the peak temperature and peak pressure attained during the evolution. In particular, the maximum temperature is appreciably lower when air chemistry is included. Also, the stiffened EOS inside the bubble increases the stiffness of the bubble, thereby significantly increasing the radius at the time of rebound, which in turn reduces the peak bubble pressure by an order of magnitude. We comment that the peak temperature and peak pressure in the simulations of Ref. [19], without air chemistry and high pressure EOS, are on the order of 100 eV and 10^4 GPa, respectively. Here the peak temperature for case A is on the order of 1 eV, which is closer to that observed in sonoluminescence [6], and the peak pressure is on the order of 100 GPa.

Note that the switch between ideal and stiffened gas EOS is currently binary; i.e., the stiffened EOS is turned on once the maximum pressure inside the bubble reaches 1 GPa. This occurs at a time of approximately ~46 ns, which causes a "kink" in the evolution of maximum temperature and maximum pressure in case A. A unified EOS, or one with a smoother transition, will be sought in the future.

B. Shock bubble interaction

1. Overall dynamics

We next carry out numerical simulations of shock-induced axisymmetric bubble collapse in water. The imposed postshock pressure is 10 GPa, and the initial diameter of the bubble is taken to be 30 μm. The computational domain is $r = [0{:}100]$ μm in the radial direction, and $x = [-100{:}100]$ μm in the streamwise direction. A grid resolution study is performed first, and we include both the stiffened gas EOS and air chemistry in these simulations. Figure 6 plots the mass-averaged pressure, mass-averaged u velocity, and maximum temperature of the bubble as well as the maximum pressure in the water as a function of time and for different grid resolutions. Here the mass-averaged quantities

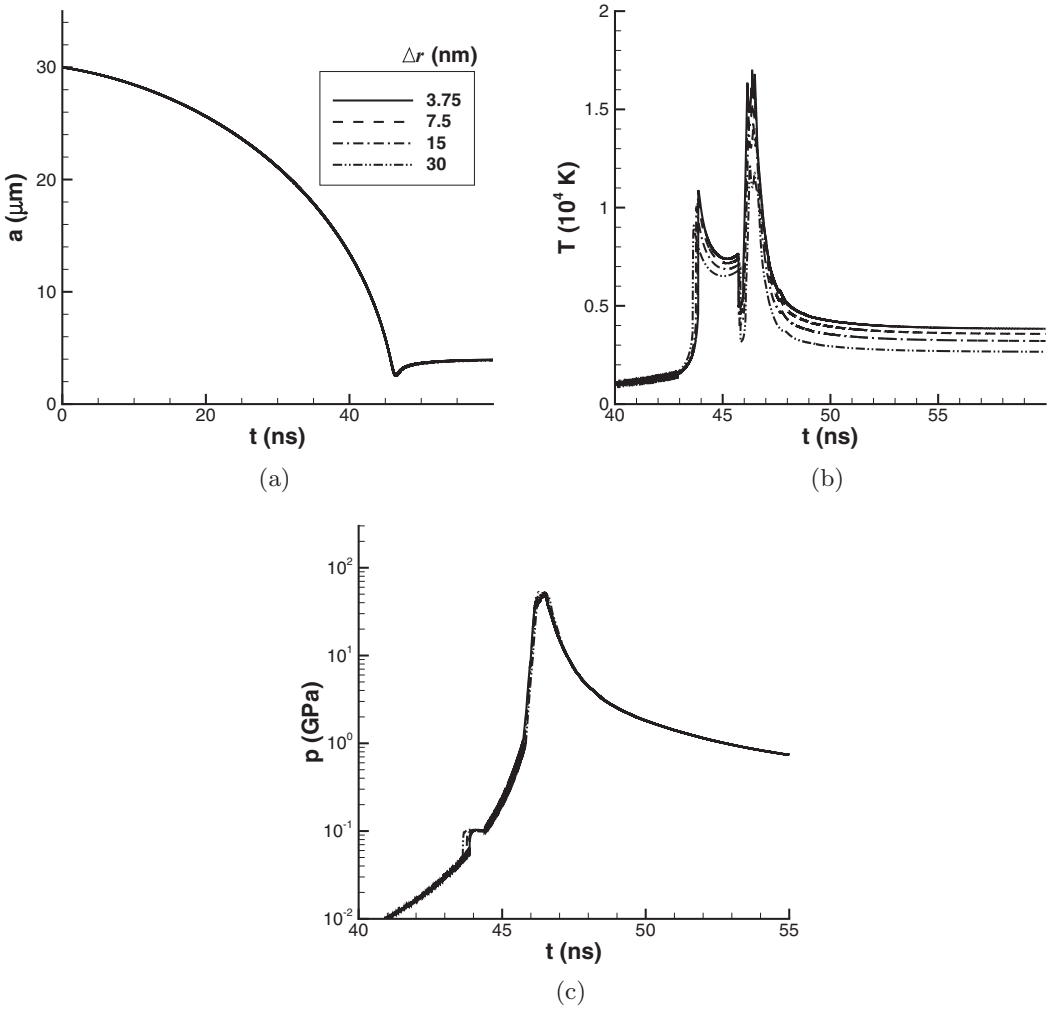

FIG. 3. Plot of (a) radius, (b) maximum temperature (in 10^4 K $\sim$ 1 eV), and (c) maximum pressure as a function of time and for grid resolutions of $\Delta r = 3.75$ (solid), 7.5 (dash), 15 (dash-dot), and 30 (dash-dot-dot) nm. Note that the time axes are different.

are defined by

$$(\cdot)_{b,m} = \int_{m_b} (\cdot) dm = \frac{\int_{\mathcal{V}_b} \rho(\cdot)\, d\mathcal{V}}{\int_{\mathcal{V}_b} \rho\, d\mathcal{V}} = \frac{\int_{\mathcal{V}} \phi\rho(\cdot)\, d\mathcal{V}}{\int_{\mathcal{V}} \phi\rho\, d\mathcal{V}}, \tag{29}$$

where $\mathcal{V}_b$ denotes the volume of the bubble and $\mathcal{V}$ denotes the volume of the computational domain. Thus, the mass-averaged pressure is defined as

$$p_{b,m} = \frac{\int_{\mathcal{V}} (\phi\rho p)\, d\mathcal{V}}{\int_{\mathcal{V}} (\phi\rho)\, d\mathcal{V}}. \tag{30}$$

Note that the maximum pressure inside the bubble does not reach 1 GPa, and so the stiffened gas EOS is not turned on. From the figure we see that the numerical solution converges as the grid is refined, except for late times when the bubble reaches its maximum distortion. Numerical solutions

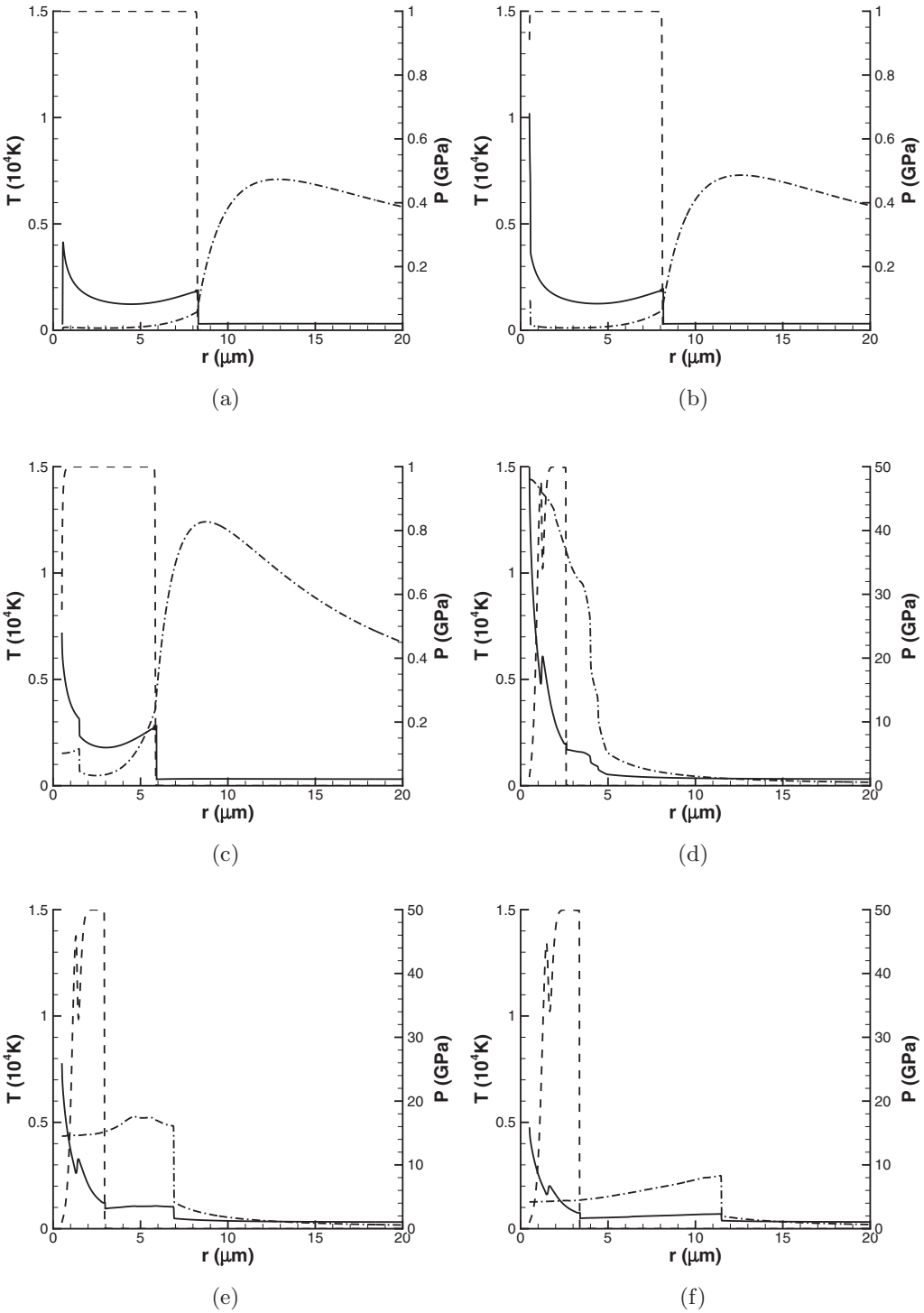

FIG. 4. Plot of temperature (solid), pressure (dash-dot), and mass fraction of O_2 (dash; between 0 and 0.23) as a function of x at times (a) $t = 43.8$, (b) 43.9, (c) 45, (d) 46.5, (e) 47, and (f) 48 ns. The grid resolution corresponds to the $\Delta r = 7.5$ nm case shown in Fig. 3. Note that panel (b) corresponds to the time when the shock reaches $r_0 = 0.05$ μm, and panel (d) when the bubble rebounds.

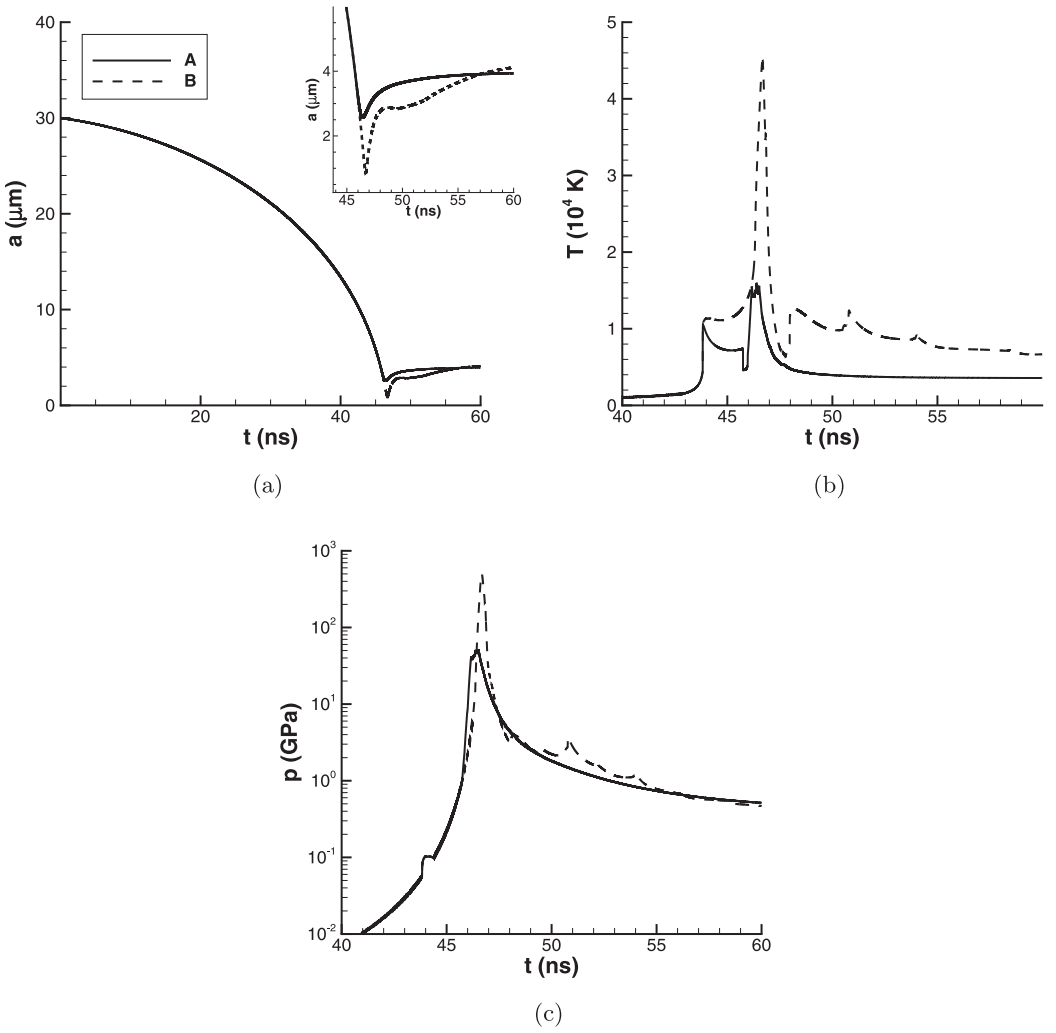

FIG. 5. Evolution of (a) radius with an inset showing the evolution near the collapse, (b) maximum temperature, and (c) maximum pressure for bubble collapse in spherical symmetry and for case A (solid) and case B (dash).

for later times requires an even finer mesh, perhaps on the order of 10 nm, or the use of adaptive-mesh refinement (AMR). We are currently working on AMR and will report results at a later date.

To examine the effect of air chemistry at high temperature inside the bubble, we first show in Fig. 7 contour plots of temperature at various times. The left column corresponds to case A, and the right column corresponds to case B. As in the previous section, case A includes both stiffened gas EOS at high pressure and air chemistry, whereas case B does not. The temperatures inside the bubble for case A (with air chemistry) are appreciably lower than those of case B (without air chemistry), showing the effect of dissociation of air molecules. Note that the relatively sharp increase in mean pressure and the start of a slowdown of the bubble velocity seen in Fig. 6 at around $t = 11$ ns is at the moment when the frontal and distal sides of the bubble collide, and a torus starts to form, as seen in the third row of Fig. 7. Figure 8 further shows the comparison of the evolution of mass-averaged pressure and maximum temperature for the two cases. The effect of air chemistry on the maximum temperature is apparent, and the effect on pressure is appreciable. Finally, the pressure in the water

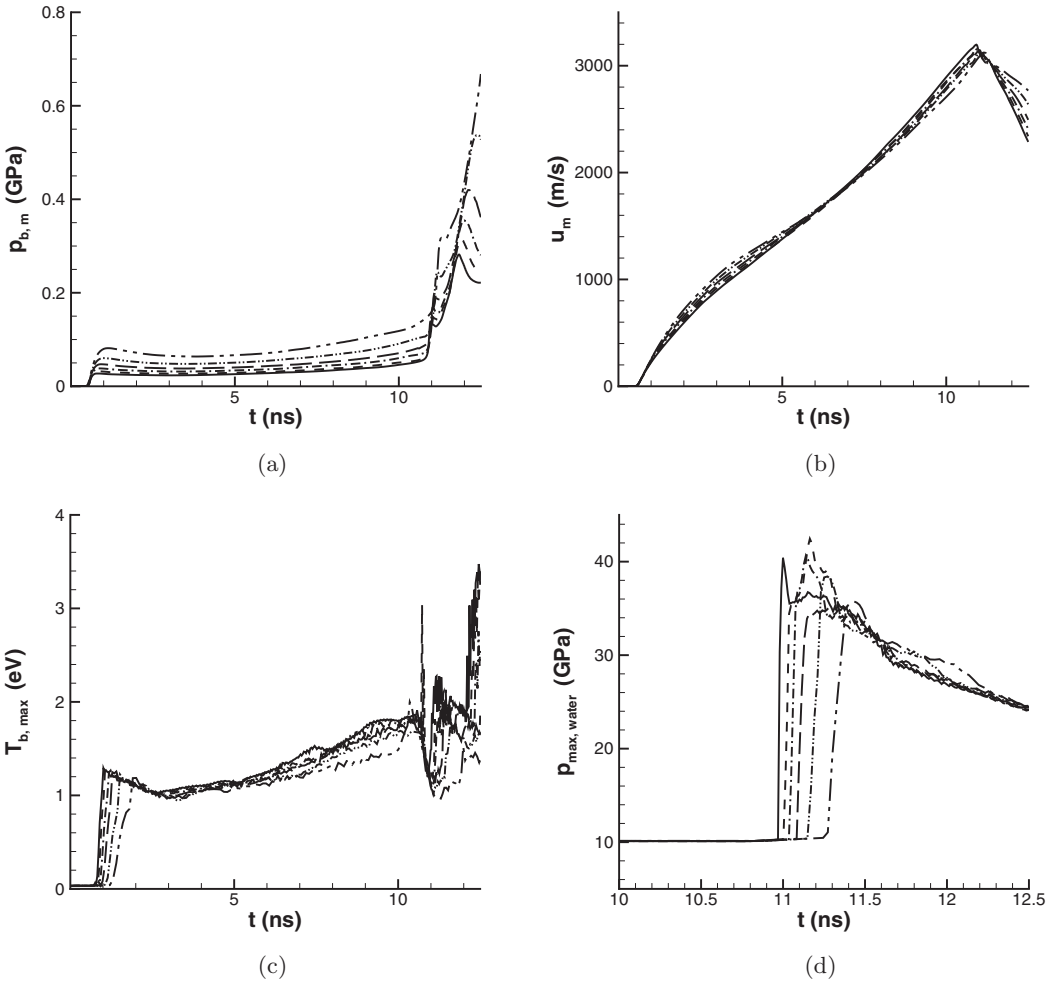

FIG. 6. Plot of (a) mass-averaged pressure, (b) mass-averaged u velocity, (c) maximum temperature (in eV) of the bubble, and (d) maximum pressure in the water as a function of time corresponding to shock-induced bubble collapse in axisymmetric geometry and for different grid resolutions. The resolutions are $d_b/360$ (long-dash-dot-dot), $d_b/480$ (dash-dot-dot), $d_b/600$ (long-dash), $d_b/720$ (dash-dot), $d_b/840$ (dash), and $d_b/960$ (solid), with d_b being the initial diameter of the bubble. In all cases, $\Delta r = \Delta x$. Note the finest mesh presented here corresponds to 31.25 nm. Here $p_{\text{shock}} = 10$ GPa.

is often of interest for cavitation erosion, and so we plot the maximum pressure in the water in Fig. 9 for the two cases. Note that there is an appreciable $\sim$8% increase in the maximum pressure experienced by the water as the frontal and distal side of the bubble collide for case A as compared to case B.

2. Effect of shock pressure

To examine the effect of shock pressure, we next perform a simulation with an imposed postshock pressure of 20 GPa. Figure 10 shows the comparison of the evolution of mass-averaged pressure and maximum temperature for the two cases. Again, case A includes both stiffened gas EOS at high pressure and air chemistry, whereas case B does not. We first note that with a stronger shock pressure p_s of 20 GPa, the frontal and distal sides of the bubble collide at an earlier time of $t = 7.7$ ns than

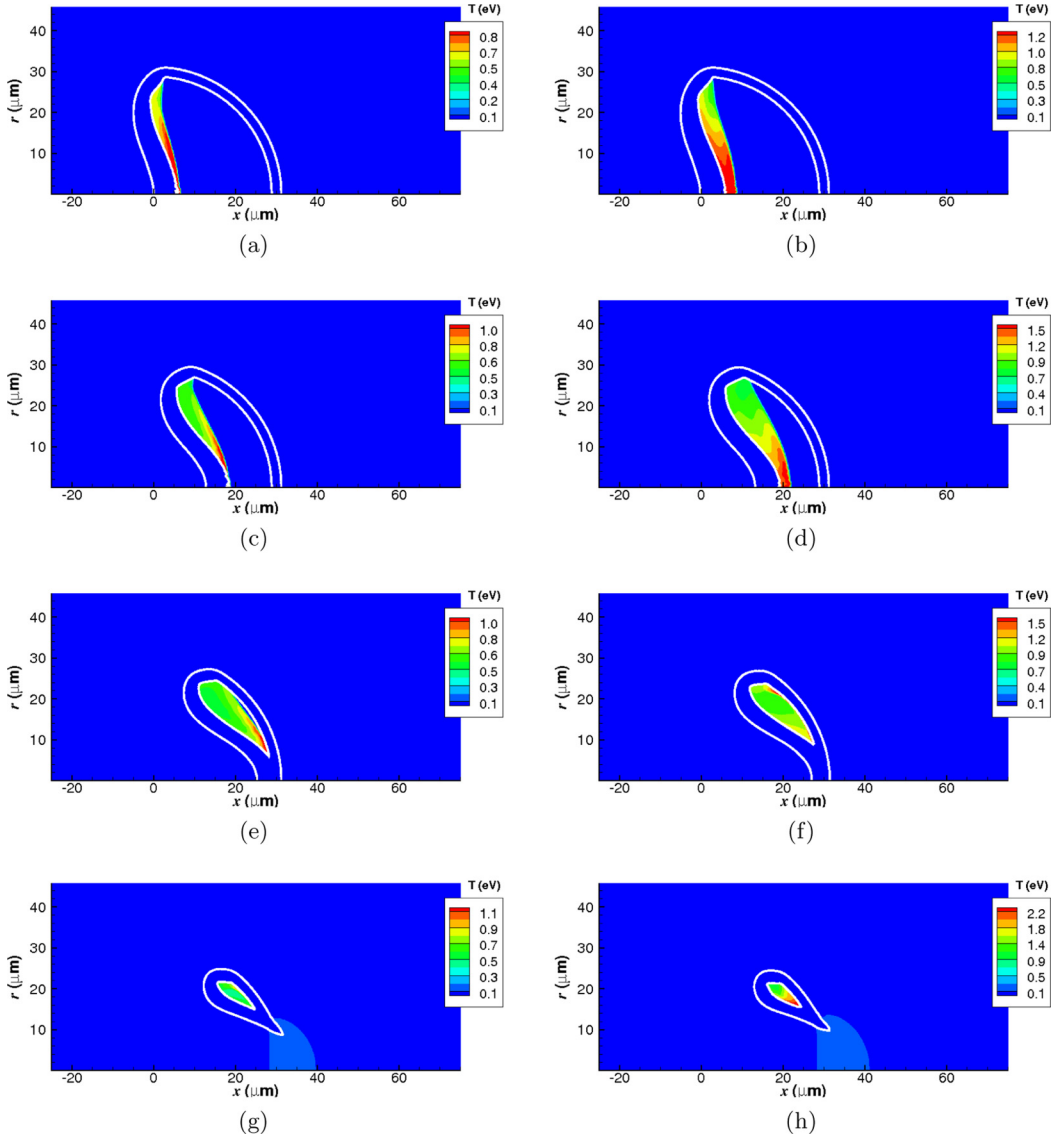

FIG. 7. Contour plots of temperature (in eV) at various times corresponding to bubble collapse in water in axisymmetric geometry. The left column corresponds to case A and the right column to case B. Times shown are (a)–(b) 7.3, (c)–(d) 9.2, (e)–(f) 11, and (g)–(h) 12.5 ns. The water-air interface is indicated by the white curve. Note that the contour levels are different for the left and right columns. Here $d_b/480$, $p_{\text{shock}} = 10$ GPa.

the previous cases with p_s of 10 GPa. The pressure inside the bubble now reaches the threshold of 1 GPa so that stiffened EOS is on. Similar to the SBSL simulations, due to the increased stiffness of the bubble, the bubble in case A does not shrink as much as in case B, and thus the pressure inside the bubble is significantly reduced. The effect of air chemistry on the maximum temperature is still apparent just like for p_s of 10 GPa. The pressure in the water is next shown in Fig. 11 for the two cases. Unlike for $p_s = 10$ GPa, the difference in the maximum pressure, between case A and case B, experienced by the water as the frontal and distal side of the bubble collide is negligible here, indicating less influence of bubble dynamics on water pressure at large shock pressure.

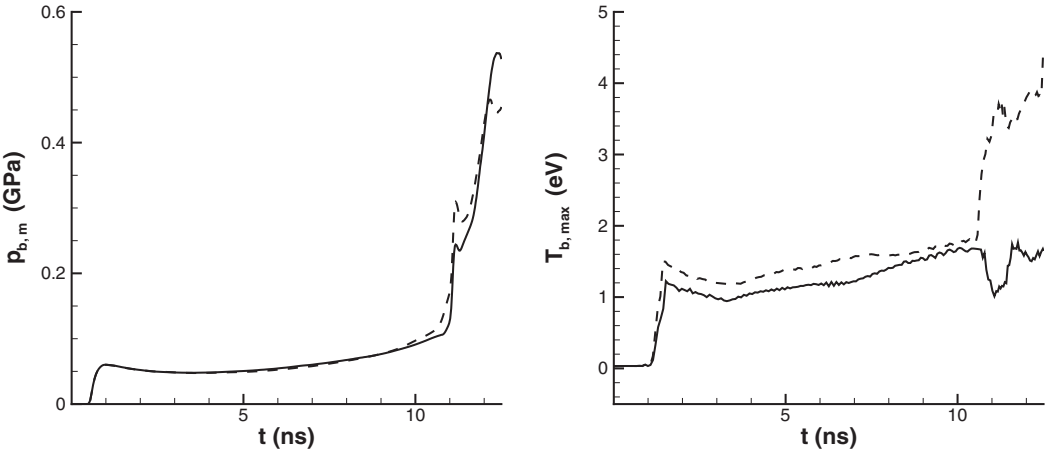

FIG. 8. Plot of (a) mass-averaged pressure and (b) maximum temperature of shock-induced bubble collapse in axisymmetric geometry for case A (solid) and case B (dash). Here $d_b/480$, $p_{\text{shock}} = 10$ GPa.

3. Effect of multiple bubble interaction

We finally examine the evolution when there are multiple bubbles. Since the simulations are currently axisymmetric, we consider two bubbles in a one-dimensional array aligned in the flow direction. The separation distance d_s is defined as the distance between the two centers. The shock pressure is taken to be 10 GPa, and the bubble radius 30 μm with separation distances d_s of ∞, 2, 1.5, and 1.25 times the bubble diameter (d_b). Thus, the separation between the distal side of the first bubble and the frontal side of the second bubble are ∞, 1, 0.5, and 0.25 diameter, respectively.

Figure 12 plots the maximum pressure and temperature in the bubble as a function of time and for the four different separation distances, while Fig. 13 plots the evolutions of maximum pressure in the water. At early times the dynamics is governed by the collapse of the first bubble as the imposed shock wave passes through it and is therefore independent of the separation distance. Thus,

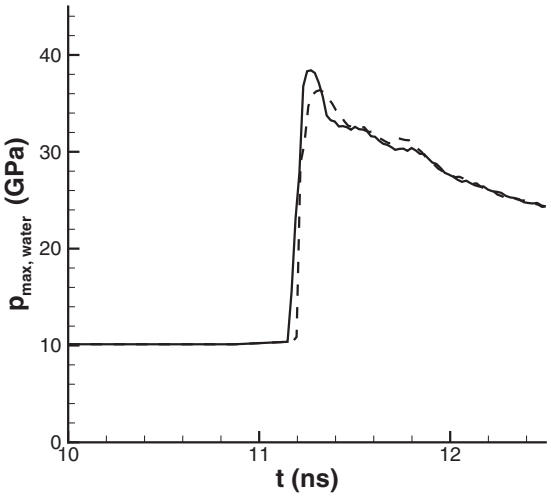

FIG. 9. Evolution of the maximum pressure in the water of shock-induced bubble collapse in axisymmetric geometry for case A (solid) and case B (dash). Here $d_b/480$, $p_{\text{shock}} = 10$ GPa.

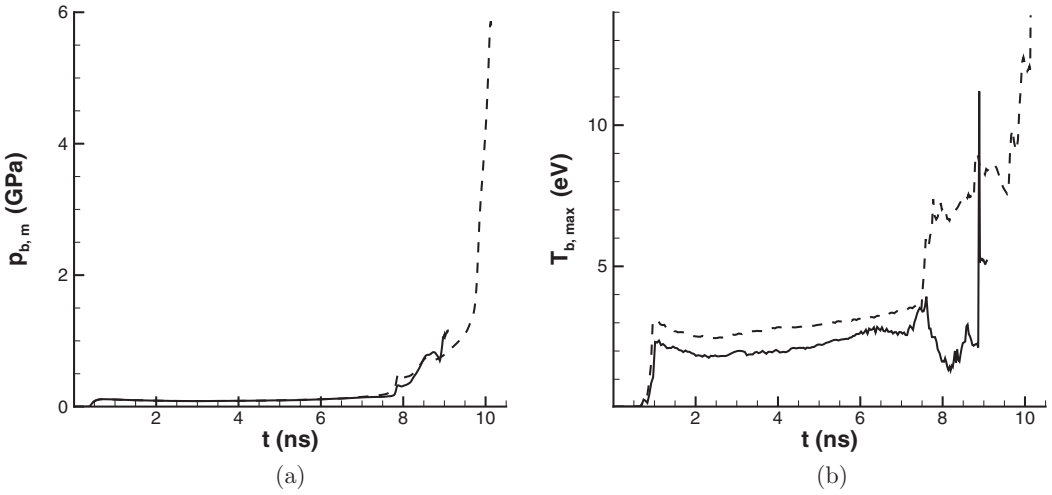

FIG. 10. Plot of (a) mass-averaged pressure and (b) maximum temperature of shock-induced bubble collapse in axisymmetric geometry for case A (solid) and case B (dash). Here $d_b/480$, $p_{\text{shock}} = 20$ GPa.

in the latter figure the peak in the maximum pressure in the water at 11 ns is due to the collision of the frontal and distal sides of the first bubble, as previously discussed in Sec. IV B 1. The peak at $t = 17$ ns in all four cases is due to the focusing of the shock generated after the first bubble collapses. This can be better appreciated by examining the dynamics exhibited by the contour plots at 16.1 and 17.3 ns in Fig, 14 for the $d_s = 2d_b$ case. In particular, the high pressure spot at $x = 25$ μm and just above the x axis travels towards the centerline, causing a high-pressure peak in the water, which has important implications to cavitation erosion. Note that the second peak is due to the late evolution of the first bubble and not a multiple bubble effect. Also, note that this high pressure generated due to the focusing of the shock wave was also observed in [38,39] for void collapse in a condensed phase.

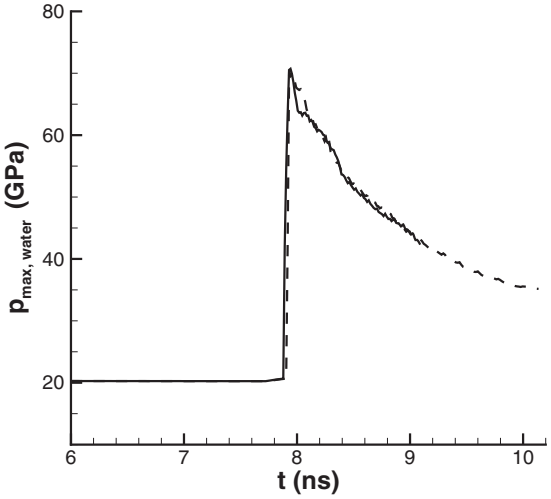

FIG. 11. Evolution of the maximum pressure in the water of shock-induced bubble collapse in axisymmetric geometry for case A (solid) and case B (dash). Here $d_b/480$, $p_{\text{shock}} = 20$ GPa.

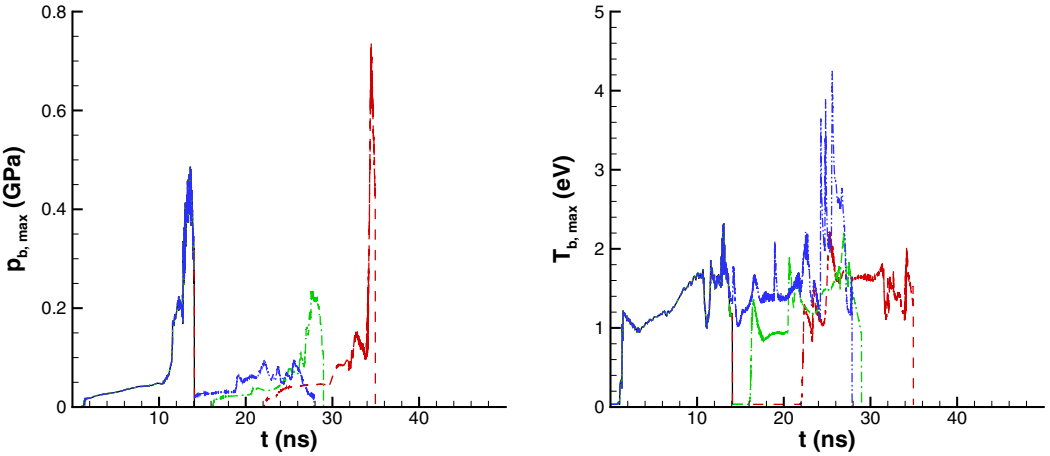

FIG. 12. Plot of (a) maximum pressure and (b) maximum temperature of shock-induced bubble collapse in axisymmetric geometry for shock two-bubble interaction for $d_s = \infty$ (solid), 2 (dash), 1.5 (dash-dot), and $1.25d_b$ (dash-dot-dot). Here $d_b/480$, $p_{\text{shock}} = 10$ GPa. Note that the solid curve overlaps with the rest up to 14 ns when the first bubble collapses, and both $p_{b,\max}$ and $T_{b,\max}$ then drop to zero since it is the only bubble.

For later times, the effect of bubble interaction starts to show up. In Fig. 13 the peaks associated with frontal-distal-side-collision for the second bubble are marked with a reference number 1, while the peaks associated with the left running shock wave generated as a result of bubble collapse are marked with a reference number 2. From the figure we see that the pressure jump at the moment of frontal-distal-side-collision for the first (at 11 ns) and second bubble (at 32 ns denoted as peak C1) follow the same distinct or instantaneous pattern for $d_s = 2d_b$ case, whereas those for the second bubble—peak A1 for $d_s = 1.25d_b$ and peak B1 for $d_s = 1.5d_b$ case—are appreciably influenced by the collapse of the first bubble. That is, as the bubbles come closer to each other, the interaction leads to a more gradual pressure rise for A1 and B1 as compared to C1. This interaction is illustrated in Fig. 15 for the $d_s = 1.5d_b$ case. The influence of the collapse of the first bubble on that of the second

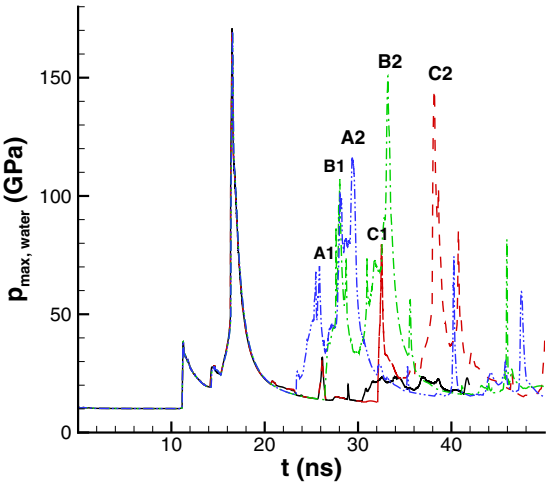

FIG. 13. Evolution of the maximum pressure in the water for shock two-bubble interaction for $d_s = \infty$ (solid), 2 (dash), 1.5 (dash-dot), and $1.25d_b$ (dash-dot-dot). Here $d_b/480$, $p_{\text{shock}} = 10$ GPa.

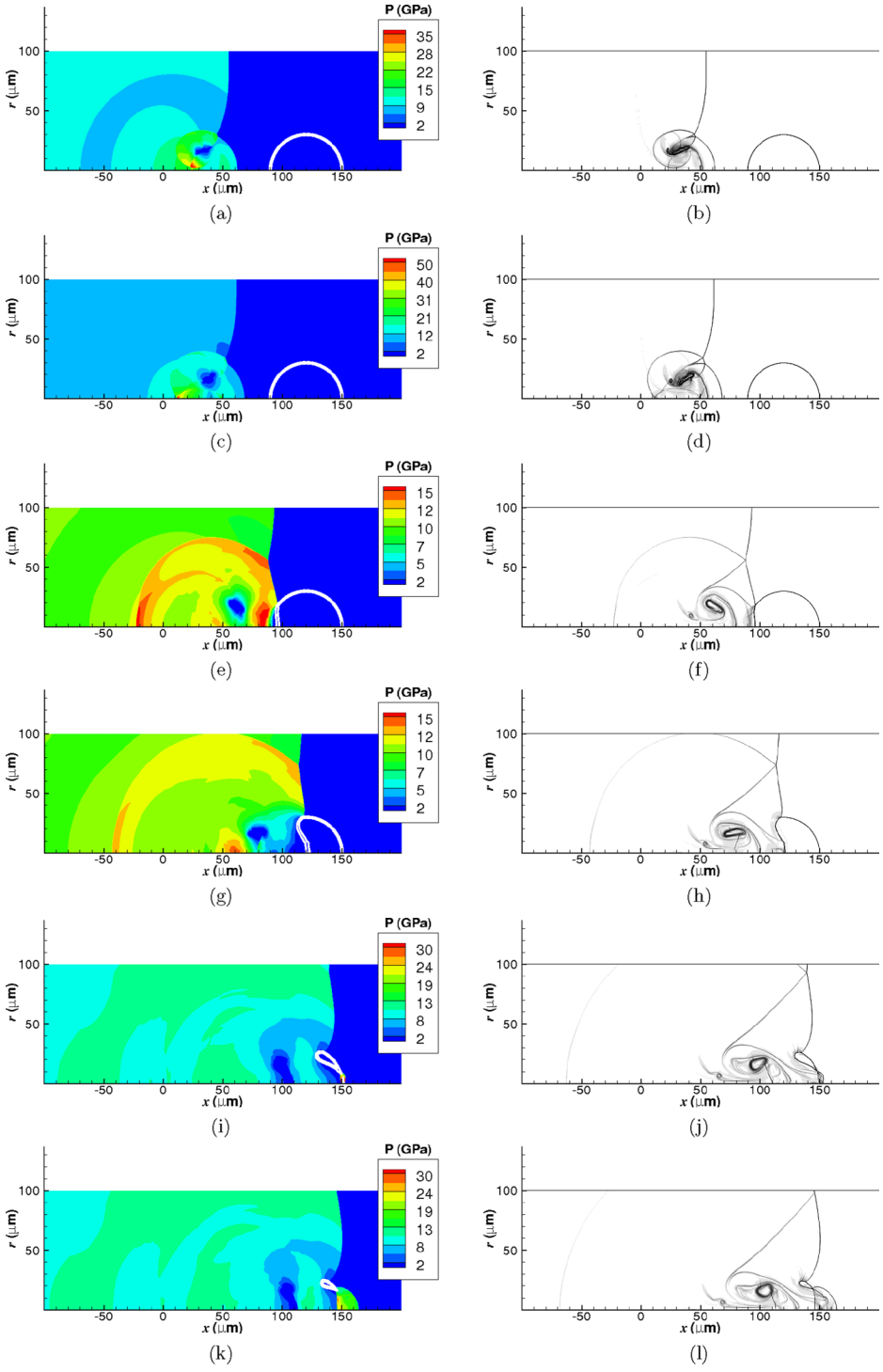

FIG. 14. Contour plots of pressure (left) and Schlieren image (right) at various times corresponding to $d_s = 2d_b$ shock two-bubble interaction in water in axisymmetric geometry. Times shown are (a)–(b) 16.1, (c)–(d) 17.3, (e)–(f) 23.2, (g)–(h) 27.7, (i)–(j) 32.4, and (k)–(l) 33.7 ns. The water-air interface is indicated by the white curve. Here $d_b/480$, $p_{\text{shock}} = 10$ GPa.

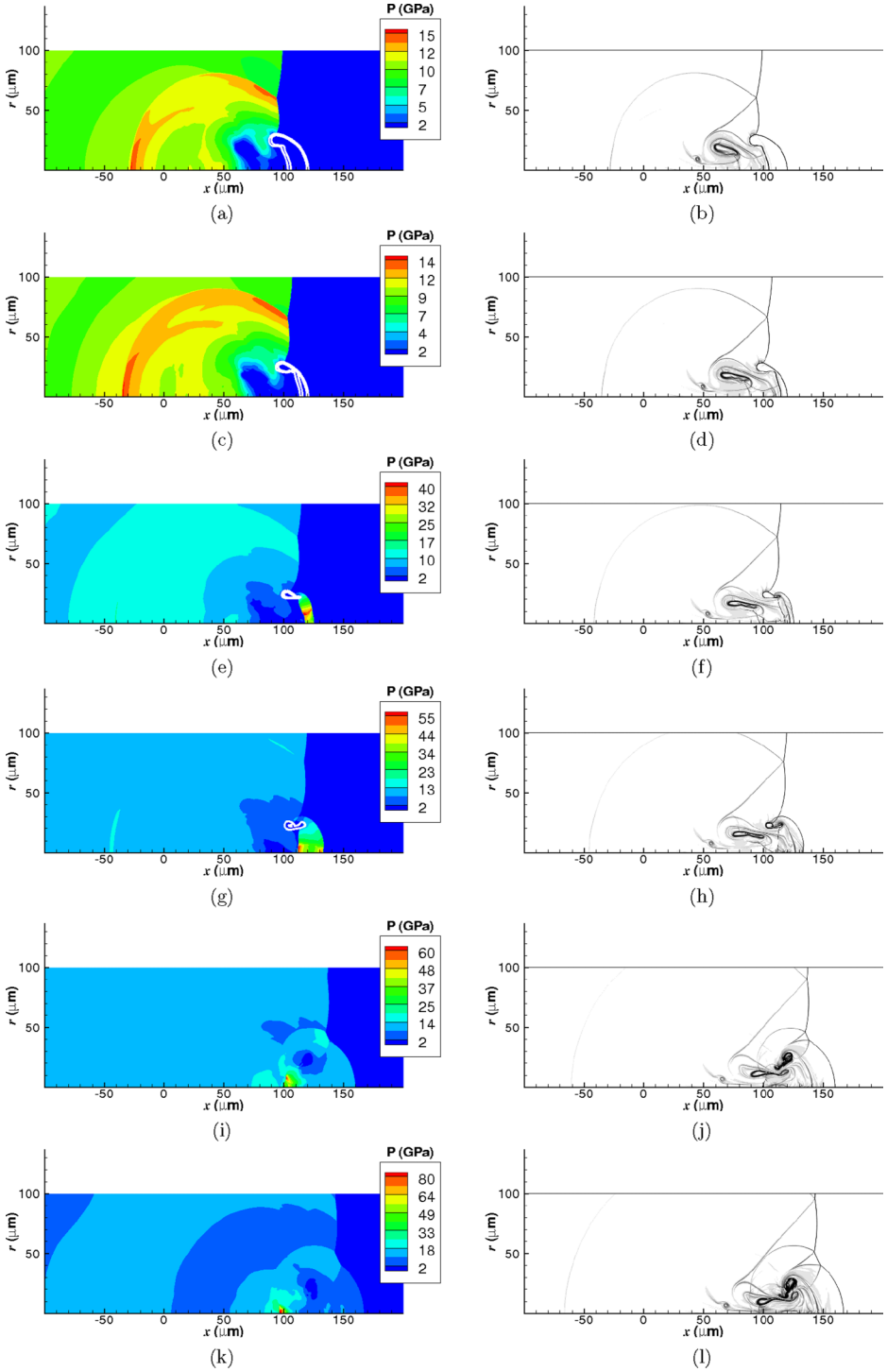

FIG. 15. Contour plots of pressure (left) and Schlieren image (right) at various times corresponding to $d_s = 1.5d_b$ shock two-bubble interaction in water in axisymmetric geometry. Times shown are (a)–(b) 24.2, (c)–(d) 26, (e)–(f) 27.5, (g)–(h) 28.6, (i)–(j) 32, and (k)–(l) 33.3 ns. The water-air interface is indicated by the white curve. Here $d_b/480$, $p_{\text{shock}} = 10$ GPa.

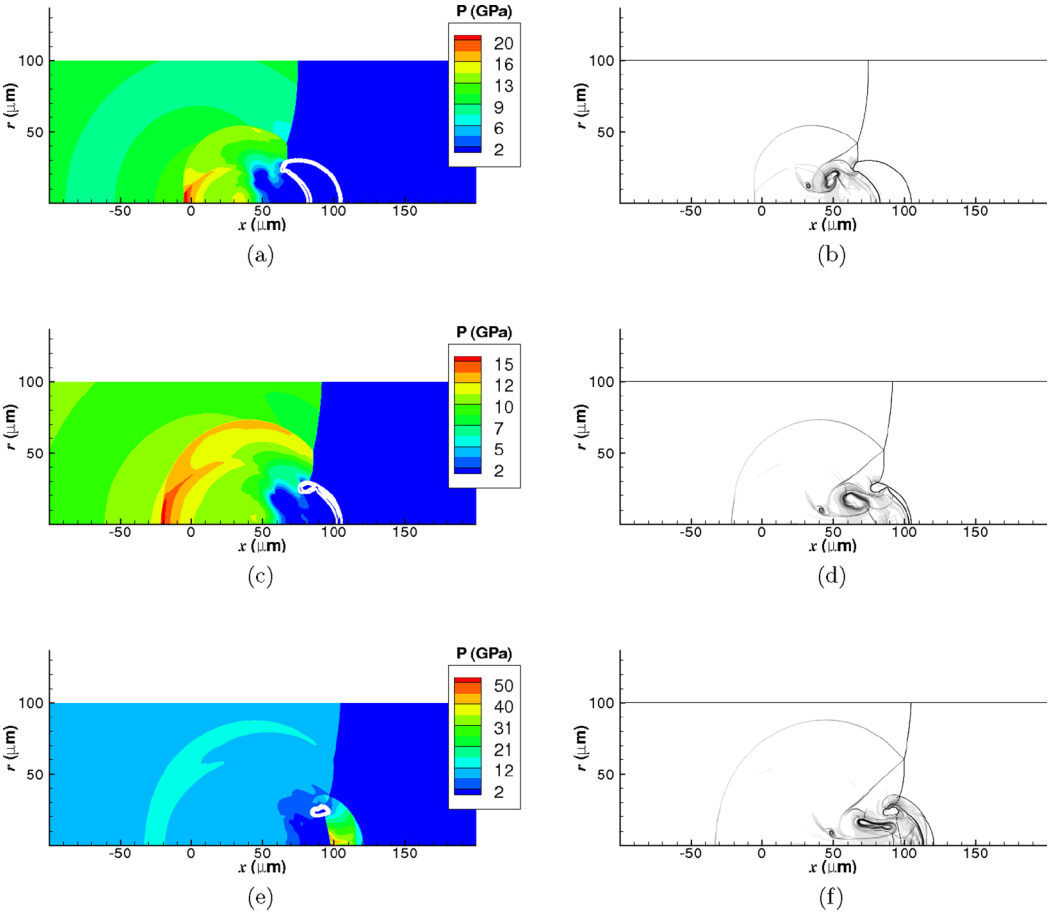

FIG. 16. Contour plots of pressure (left) and Schlieren image (right) at various times corresponding to $d_s = 1.25d_b$ shock two-bubble interaction in water in axisymmetric geometry. Times shown are (a)–(b) 19.8, (c)–(d) 23, and (e)–(f) 25.5 ns. The water-air interface is indicated by the white curve. Here $d_b/480$, $p_{\text{shock}} = 10$ GPa.

due to the close proximity of the two bubbles can be appreciated by comparing the first three rows in Fig. 15 with the last three rows in Fig. 14 at similar stages of the evolution. Note that the vortex generated by the collapse of the first bubble is much closer to the second bubble for the $d_s = 1.5d_b$ case. This vortex then accelerates and pinches the frontal side of the second bubble, leading to a stronger frontal-distal-side-collision and thus a significantly stronger peak B1 in Fig. 13 at around 28 ns than peak C1 at around 32 ns for $d_s = 2d_b$ case. When the two bubbles are even closer, like in the $d_s = 1.25d_b$ case denoted by A1, the peak pressure decreases. This is presumably due to the insufficient time for momentum to accumulate in the interaction. The evolution is illustrated in Fig. 16 for the $d_s = 1.25d_b$ case. The collapse of the second bubble is seen to generate peak pressures lower than both the $d_s = 1.5d_b$ and $d_s = 2d_b$ cases. The fact that the magnitude at B1 is larger than that for A1 and C1 indicates that there is a critical value of the separation distance where the pressure in the water associated with frontal-distal-side collision of the second bubble reaches a maximum.

Finally, the peaks A2–C2, subsequent to A1–C1, are due to the left running shock wave generated at the frontal-distal-side-collision of the second bubble. To illustrate the dynamics, Figs. 15(g)–15(h) for $d_s = 1.5d_b$ shows that there are two shocks generated at the frontal-distal-side-collision of the second bubble, the right-running one becomes weaker and weaker due to expansion, whereas the

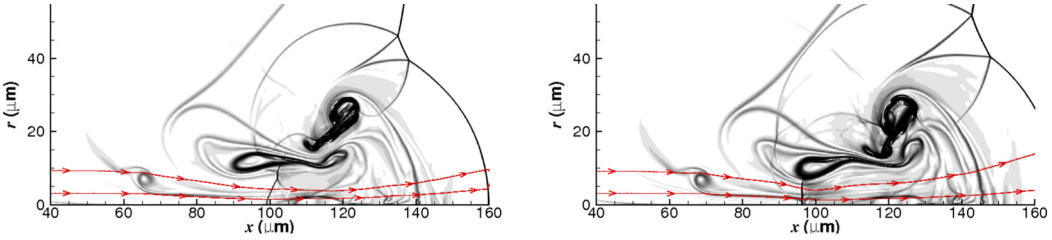

FIG. 17. Schlieren images at various times corresponding to $d_s = 1.5d_b$ shock two-bubble interaction in water in axisymmetric geometry. Streamlines are shown by arrow lines. Times shown are (a) 32 and (b) 33.3 ns, close-up view of (j) and (l) in Fig. 15, respectively.

left-running one travels upstream and gets stronger with time. There is also compression of the water near the centerline by the vortex generated by the collapse of the bubble as more clearly seen in Fig. 17, which also strengthens the left-running shock. Note the left-running shock is located at $x = \sim 100$ μm at 32 ns and ~ 95 μm at 33.3 ns.

V. DISCUSSION

To gain insight into reaction time scales at different stages of bubble collapse, we focus on and take the dissociation of H_2O and O_2 in [12] as examples, i.e.,

$$H_2O + M \rightarrow HO + O + M \tag{31}$$

and

$$O_2 + M \rightarrow 2O + M, \tag{32}$$

with reaction rate coefficient defined as

$$R_f = A_f T^{b_f} e^{-C_f/T}, \tag{33}$$

with parameters listed in Table III.

The reaction rate coefficient, R_f, as a function of temperature for H_2O and O_2 dissociation are plotted in Fig. 18. We first note that the reaction rate coefficient for O_2 dissociation in the current work is a factor of ~ 2 different from that in Ref. [12]. Considering the error bar on the order of less than one order of magnitude for reaction rate data as noted in Ref. [12], this comparison serves as a cross-validation of the kinetic parameters in the current work.

We now examine the reaction time scales defined as

$$t_r = [X]/R_f \tag{34}$$

at different stages of bubble collapse in Fig. 2(a) of Ref. [12]. We first calculate the reaction time scale at the instant of time of 31 μs with temperature on the order of a few hundred Kelvin, bubble radius on the order of 8 μm, and H_2O concentration on the order of $10^9/N_A/V_{\text{bub}} = 0.777$ mol/m^3. Here 10^9 is the estimate of number of H_2O molecules at 31 μs based on Fig. 2(b) of Ref. [12]. Thus,

TABLE III. Kinetic parameters of H_2O and O_2 dissociation in Ref. [12].

	H_2O	O_2
A_f ($\frac{\text{m}^3\,\text{K}^{-b_f}}{\text{mol s}}$)	1.96×10^{16}	1.58×10^{11}
b_f	-1.62	-0.5
C_f (K)	59 700	59 472

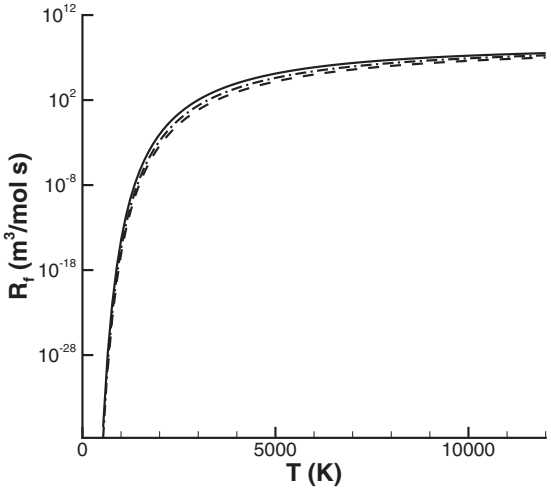

FIG. 18. Plots of reaction rate coefficient, R_f, as a function of temperature for H_2O (solid) and O_2 (dash) dissociation in Ref. [12]. The reaction rate coefficient for O_2 dissociation in the current work is also plotted as the dash-dotted line.

t_r is essentially infinite as R_f is diminishingly small as seen in Fig. 18. There would be essentially no reactions until the temperature reaches ~1300 K at ~40 ns later when t_r is on ns scale with R_f on the order of 10^{-9} $\frac{\text{m}^3}{\text{mol s}}$ and $[H_2O]$ on the order of 10 $\frac{\text{mol}}{\text{m}^3}$. Note that the result of this time scale analysis is similar for O_2 dissociation as well and is consistent with the evolution shown in Fig. 4 in the current work where reaction does not start until a few ns before the collapse. Therefore, it seems to be justifiable to neglect the evolution of bubble expansion but start a full-hydrodynamic simulation tens of ns before the collapse with rationally assumed initial conditions and chemical compositions, and bypass the stages dynamically and chemically less dramatic yet computationally much more time consuming for a full-hydrodynamic simulation. In addition, as already noted in Sec. IV A, the initial conditions are chosen to be representative of those for Step 2 in Ref. [19],

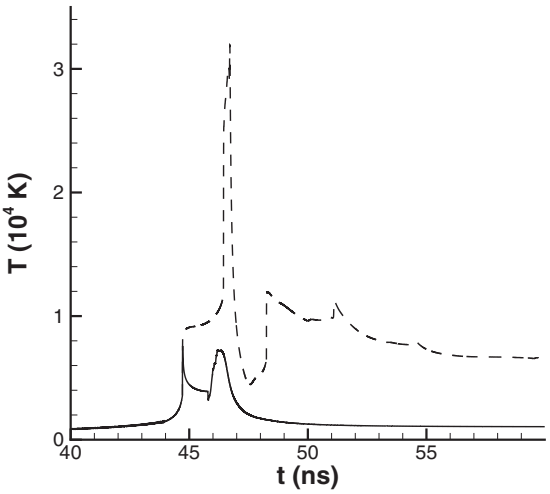

FIG. 19. Evolution maximum temperature of bubble collapse in spherical symmetry for case with H_2O dissociation and stiffened EOS at high pressure (solid) and without (dashed).

TABLE IV. Parameters of EOS for water vapor.

Parameter	Vapor ($p_{\max} \leqslant 1$ GPa)	Vapor ($p_{\max} > 1$ GPa)
ρ_0 (kg/m^3)	1	1000
γ	1.327	4.4
P^∞ (atm)	0	6000

where bubble expansion was indeed simulated in Step 1 and the results obtained from Step 1 were used as the initial conditions for Step 2 at tens of ns before the final collapse. The bubble expansion, acoustics and the associated vaporization, etc., will, however, indeed be further investigated in the future, especially when the number of H_2O molecules constantly decreases as seen in Fig. 2(b) of Ref. [12] even though there was no reaction at early times. This decrease is presumably caused by dissolution and/or evaporation and condensation.

Detailed study with H_2O chemistry fully considered will also be conducted in the future. Here as a demonstration, we show simulations in Fig. 19 for cases with and without H_2O dissociation. The simulations correspond to bubble collapse in spherical symmetry with an initial bubble radius of $R_0 = 30\ \mu$m in the water. Similar to the simulations in Sec. IV A, the initial conditions are given by

$$\rho = \rho_{\text{water}}\phi + \rho_{\text{vapor}}(1-\phi), \tag{35}$$

$$p = 10^5\ (\text{Pa}), \tag{36}$$

$$v_r = \begin{cases} 0, & \text{for} \quad r_0 \leqslant r \leqslant R_0, \\ -100\ (\text{m/s}), & \text{otherwise}, \end{cases} \tag{37}$$

$$\phi = \frac{1}{2}\left[1 + \tanh\left(\frac{r - R_0}{2\epsilon_h}\right)\right], \tag{38}$$

where ϕ is the water volume fraction. Here r is the radial coordinate in spherical coordinates. For simplicity, the bubble is assumed to be pure water vapor due to the dominance of H_2O tens of ns before collapse shown in Fig. 2(b) of Ref. [12]. Thus, the initial mass fraction of H_2O is 1. The stiffened-gas EOS parameters for water were still listed in Table I, and those for the vapor are listed in Table IV. It can be seen from Fig. 19 that vapor chemistry has a significant effect on the peak temperature attained during the evolution.

We finally comment that the time scale for thermal diffusion in the liquid water at tens of ns before the collapse can defined as

$$t_{\text{th}} = l^2/\alpha, \tag{39}$$

with l being the length scale of the bubble chosen to be the radius of the bubble and $\alpha = 0.143 \times 10^{-6}$ m^2/s the thermal diffusivity of water. This thermal diffusion time scale is on the order of 1.7 μs even at the moment of collapse when the radius of the bubble is $\sim$0.5 μm shown in Fig. 2(a) of Ref. [12]. Therefore, thermal diffusion at the evolution stage examined in the current work may be neglected.

VI. CONCLUSIONS

The combined effect of a stiffened gas EOS for air at high pressure and air chemistry at high temperatures on the evolution of bubble collapse are examined by carrying out axisymmetric simulations. It is found that when air chemistry is included in the numerical simulations of single-bubble sonoluminescence, the bubble temperature is reduced significantly and is on the

order of 1 eV, which is closer to that observed in sonoluminescence experiments. Thus, for an accurate prediction of bubble temperature, it is suggested here that air chemistry should be explicitly included in the governing equations. In addition, a stiffened-gas EOS, calibrated by shock Hugoniot data of liquid air, is used for air at high pressures, and it is found that with a stiffened EOS, the peak pressure is reduced by an order of magnitude. For a GPa-shock-induced axisymmetric bubble collapse, the pressure inside the bubble is not as high as those in single-bubble sonoluminescence, yet the effect of air chemistry on the maximum temperature is still apparent.

We also examine the effect of multiple bubble interaction in shock-induced bubble collapse, by carrying out axisymmetric simulations for two bubbles aligned in the flow direction. We find that the frontal-distal-side-collision, shock focusing, upstream-traveling shocks, and compression by vortex generated by bubble collapse can all lead to significant increase in pressure in the water. These can have important implications for cavitation erosion.

ACKNOWLEDGMENTS

This work was supported in part by the U.S. Department of Energy, National Nuclear Security Administration, Advanced Simulation and Computing Program, as a Cooperative Agreement under the Predictive Science Academic Alliance Program, under Contract No. DE-NA0002378. This work was also supported in part by the Defense Threat Reduction Agency, Basic Research Award under award No. HDTRA1-14-1-0031.

[1] D. Silberrad, Propeller erosion, Engineering **93**, 33 (1912).
[2] N. Marinesco and J. J. Trillat, Action of supersonic waves upon the photographic plate, Proc. R. Acad. Sci. **196**, 858 (1933).
[3] J. Frenzel and H. Schultes, Luminescence in water carrying supersonic waves, Z. Phys. C **27**, 421 (1934).
[4] D. F. Gaitan, L. A. Crum, C. C. Church, and R. A. Roy, Sonoluminescence and bubble dynamics for a single, stable, cavitation bubble, J. Acoust. Soc. Am. **91**, 3166 (1992).
[5] S. Hilgenfeldt, M. P. Brenner, S. Grossmann, and D. Lohse, Analysis of Rayleigh-Plesset dynamics for sonoluminescing bubbles, J. Fluid Mech. **365**, 171 (1998).
[6] K. S. Suslick, S. J. Doktycz, and E. B. Flint, On the origin of sonoluminescence and sonochemistry, Ultrasonics **28**, 280 (1990).
[7] A. Philipp and W. Lauterborn, Cavitation erosion by single laser-produced bubbles, J. Fluid Mech. **361**, 75 (1998).
[8] L. Rayleigh, VIII. On the pressure developed in a liquid during the collapse of a spherical cavity, London, Edinburgh Dublin Phil. Mag. J. Sci. **34**, 94 (1917).
[9] M. S. Plesset, The dynamics of cavitation bubbles, J. Appl. Mech. **16**, 277 (1949).
[10] W. Lauterborn and T. Kurz, Physics of bubble oscillations, Rep. Prog. Phys. **73**, 106501 (2010).
[11] K. Yasui, Alternative model of single-bubble sonoluminescence, Phys. Rev. E **56**, 6750 (1997).
[12] K. Yasui, T. Tuziuti, M. Sivakumar, and Y. Iida, Theoretical study of single-bubble sonochemistry, J. Chem. Phys. **122**, 224706 (2005).
[13] K. Yasui, T. Tuziuti, J. Lee, T. Kozuka, A. Towata, and Y. Iida, Numerical simulations of acoustic cavitation noise with the temporal fluctuation in the number of bubbles, Ultrasonics Sonochem. **17**, 460 (2010).
[14] D. Schanz, B. Metten, T. Kurz, and W. Lauterborn, Molecular dynamics simulations of cavitation bubble collapse and sonoluminescence, New J. Phys. **14**, 113019 (2012).
[15] A. Prosperetti, Vapor bubbles, Annu. Rev. Fluid Mech. **49**, 221 (2017).
[16] K. Tsiglifis and N. A. Pelekasis, Numerical simulations of the aspherical collapse of laser and acoustically generated bubbles, Ultrasonics Sonochem. **14**, 456 (2007).

[17] A. Alhelfi and B. Sundn, A condition monitoring for collapsing bubble mechanism for sonoluminescence and sonochemistry, J. Thermal Sci. Eng. Appl. **7**, 021014 (2015).
[18] C. C. Wu and P. H. Roberts, Shock-Wave Propagation in a Sonoluminescing Gas Bubble, Phys. Rev. Lett. **70**, 3424 (1993).
[19] W. C. Moss, D. B. Clarke, J. W. White, and D. A. Young, Hydrodynamic simulations of bubble collapse and picosecond sonoluminescence, Phys. Fluids **6**, 2979 (1994).
[20] M. Koch, C. Lechner, F. Reuter, K. Kohler, R. Mettin, and W. Lauterborn, Numerical modeling of laser generated cavitation bubbles with the finite volume and volume of fluid method, using OpenFOAM, Comput. Fluids **126**, 71 (2016).
[21] N. A. Hawker and Y. Ventikos, Interaction of a strong shockwave with a gas bubble in a liquid medium: A numerical study, J. Fluid Mech. **701**, 59 (2012).
[22] B. Tully, N. Hawker, and Y. Ventikos, Modeling asymmetric cavity collapse with plasma equations of state, Phys. Rev. E **93**, 053105 (2016).
[23] E. Johnsen and T. Colonius, Shock-induced collapse of a gas bubble in shockwave lithotrispy, J. Acoust. Soc. Am. **124**, 2011 (2008).
[24] E. Johnsen and T. Colonius, Numerical simulations of non-spherical bubble collapse, J. Fluid Mech. **629**, 231 (2009).
[25] G. L Schott, Measured Hugoniot states of a two-elements fluid, $O_2 + N_2$, near 2 Mg/m^3, in *Shock Waves in Condensed Matter*, edited by J. R. Asay, R. A. Graham, and G. K. Straub (North-Holland, Amsterdam, 1984), p. 49.
[26] E. F. Toro, *Riemann Solvers and Numerical Methods for Fluid Dynamics* (Springer, Berlin, 1997).
[27] E. F. Toro, M. Spruce, and W. Speares, Restoration of the contact surface in the HLL-Riemann solver, Shock Waves **4**, 25 (1994).
[28] S. Gottlieb and C. W. Shu, Total variation diminishing Runge-Kutta schemes, Math. Comput. **67**, 73 (1998).
[29] R. Shukla, C. Pantano, and J. Freund, An interface capturing method for the simulation of multi-phase compressible flows, J. Comput. Phys. **229**, 7411 (2010).
[30] J. Zhang, T. L. Jackson, J. Buckmaster, and J. B. Freund, Numerical modeling of shock-to-detonation transition in energetic materials, Combust. Flame **159**, 1769 (2012).
[31] A. Tiwari, J. B. Freund, and C. Pantano, A diffuse interface model with immiscibility preservation, J. Comput. Phys. **252**, 290 (2013).
[32] R. K. Shukla, Nonlinear preconditioning for efficient and accurate interface capturing in simulation of multicomponent compressible flows, J. Comput. Phys. **276**, 508 (2014).
[33] P. Sridharan, T. L. Jackson, J. Zhang, and S. Balachandar, Shock interaction with one-dimensional array of particles in air, J. Appl. Phys. **117**, 075902 (2015).
[34] G. Allaire, S. Clerc, and S. Kokh, A five-equation model for the simulation of interfaces between compressible fluids, J. Comput. Phys. **181**, 577 (2002).
[35] J. D. Anderson, *Hypersonic and High Temperature Gas Dynamics*, 2nd ed. (AIAA, Reston, VA, 2006).
[36] C. Borgnakke and R. E. Sonntag, *Fundamentals of Thermodynamics*, 8th ed. (John Wiley & Sons, New York, 2013).
[37] J. B. Keller and M. Miksis, Bubble oscillations of large amplitude, J. Acoust. Soc. Am. **68**, 628 (1980).
[38] M. Ozlem, D. W. Schwendeman, A. K. Kapila, and W. D. Henshaw, A numerical study of shock-induced cavity collapse, Shock Waves **22**, 89 (2012).
[39] A. K. Kapila, D. W. Schwendeman, J. R. Gambino, and W. D. Henshaw, A numerical study of the dynamics of detonation initiated by cavity collapse, Shock Waves **25**, 545 (2015).